Lamina-Specific Anatomic Magnetic Resonance Imaging of the Human Retina

Yi Zhang,[1,2,3] *Oscar San Emeterio Nateras,*[1,2,3] *Qi Peng,*[1,2,3] *Roman V. Kuranov,*[4] *Joseph M. Harrison,*[4] *Thomas E. Milner,*[5] *and Timothy Q. Duong*[1,2,4,6,7]

Purpose. Magnetic resonance imaging (MRI) of the human retina faces two major challenges: eye movement and hardware limitation that could preclude human retinal MRI with adequate spatiotemporal resolution. This study investigated eye-fixation stability and high-resolution anatomic MRI of the human retina on a 3-Tesla (T) MRI scanner. Comparison was made with optical coherence tomography (OCT) on the same subjects.

Methods. Eye-fixation stability of protocols used in MRI was evaluated on four normal volunteers using an eye tracker. High-resolution MRI ($100 \times 200 \times 2000$ μm) protocol was developed on a 3-T scanner. Subjects were instructed to maintain stable eye fixation on a target with cued blinks every 8 seconds during MRI. OCT imaging of the retina was performed. Retinal layer thicknesses measured with MRI and OCT were analyzed for matching regions of the same eyes close to the optic nerve head.

Results. The temporal SDs of the horizontal and vertical displacements were 78 ± 51 and 130 ± 51 μm ($\pm$SD, $n = 4$), respectively. MRI detected three layers within the human retina, consistent with MRI findings in rodent, feline, and baboon retinas. The hyperintense layer 1 closest to the vitreous likely consisted of nerve fiber, ganglion cell, and inner nuclear layer; the hypointense layer 2, the outer nuclear layer and the inner and outer segments; and the hyperintense layer 3, the choroid. The MRI retina/choroid thickness was 711 ± 37 μm, 19% ($P < 0.05$) thicker than OCT thickness (579 ± 34 μm).

Conclusions. This study reports high-resolution MRI of lamina-specific structures in the human retina. These initial results are encouraging. Further improvement in spatiotemporal resolution is warranted. (*Invest Ophthalmol Vis Sci.* 2011;52:7232–7237) DOI:10.1167/iovs.11-7623

From the [1]Research Imaging Institute and the Departments of [2]Radiology, [4]Ophthalmology, and [6]Physiology, University of Texas Health Science Center, San Antonio, Texas; [5]Department of Biomedical Engineering, The University of Texas at Austin, Austin, Texas; and [7]South Texas Veterans Health Care System, San Antonio, Texas.

[3]These authors contributed equally to the work presented here and should therefore be regarded as equivalent authors.

Supported in part by a Clinical Translational Science Award Pilot grant (TQD) and a Translational Technology Resource Grant UL1RR025767 (QP), National Institutes of Health/National Eye Institute Grants R01 EY014211 and EY018855, and Department of Veterans Affairs Merit awards (TQD).

Submitted for publication March 24, 2011; revised June 8, 2011; accepted July 4, 2011.

Disclosure: **Y. Zhang**, None; **O. San Emeterio Nateras**, None; **Q. Peng**, None; **R.V. Kuranov**, None; **J.M. Harrison**, None; **T.E. Milner**, None; **T.Q. Duong**, None

Corresponding author: Timothy Q. Duong, University of Texas Health Science Center at San Antonio, Research Imaging Institute, 8403 Floyd Curl Dr., San Antonio, TX 78229; duongt@uthscsa.edu.

The retina is highly structured and is composed of three major tissue layers: outer nuclear layer (ONL), inner nuclear layer (INL), and ganglion cell layer (GCL).[1] There are also plexiform layers that are synaptic links between these adjacent nuclear cell layers. The retina is nourished by two blood supplies: the retinal and choroidal vasculatures.[2] The retinal vasculature exists primarily within the GCL, but does project a deep planar capillary bed into the INL. The choroidal vasculature is located beneath the ONL and its segments. Thus, the ONL is completely avascular[2] and relies on diffusion from both vasculatures for the delivery of oxygen and nutrients. Many retinal diseases result in progressive damage to different retinal layers. Thus, the ability to image these anatomic layers noninvasively could help staging and ultimately improve clinical management of retinal diseases.

Most existing in vivo retinal imaging techniques use visible or near-infrared light. These include fundus photography, confocal imaging,[3] and optical coherence tomography (OCT)[4] for anatomic imaging, fluorescein angiography,[5,6] indocyanin-green angiography,[7,8] and laser-speckle imaging[9,10] for blood-flow imaging, and intrinsic optical imaging technique[11,12] and phosphorescence[13] for oximetric imaging. Although many of these optical techniques offer high spatiotemporal resolution with many clinical utilities, with the exception of OCT, optical imaging techniques are depth ambiguous. Further, disease-induced opacity of the vitreous humor, cornea, and/or lens (such as vitreous hemorrhage or cataract) could render optical imaging techniques less effective.

By contrast, magnetic resonance imaging (MRI) provides excellent soft-tissue contrast without depth limitation and has been widely used to image the brain and other organs in both research and clinical settings. In animal models, layer-specific anatomic,[10,14] relaxation time,[15,16] manganese-enhanced,[17–19] blood flow,[20–22] blood volume[23,24] MRIs and multimodal functional MRI (fMRI) of physiologic[20,21,24,25] and visual[23,26,27] stimulation of the retina have been reported. Many of these studies showed lamina-specific retinal resolution. Multimodal MRI has also been applied to study retinal degeneration,[21,25] diabetic retinopathy,[28] and glaucoma[29,30] in rodent models.

Successful translation of retinal MRI application from animals to humans must overcome two major challenges: (1) magnetic field gradients and shims on clinical scanners are less powerful compared with those on animal scanners, which can limit spatial resolution and image quality, respectively; and (2) eye motion in awake humans may preclude application of time-series fMRI of the retina and high-resolution studies where signal averaging is required. Anatomic, blood-flow, and blood-oxygenation-level dependent (BOLD) MRIs were recently applied to study the anesthetized large nonhuman primate (baboon) retina using a 3-Tesla (T) clinical scanner,[31] demonstrating that a typical clinical scanner has the hardware capability to provide high spatial resolution for studying the retina. MRI application to human retinas using anatomic MRI,[32,33] basal blood flow MRI,[34,35] BOLD[36] fMRI, and blood-flow fMRI

Investigative Ophthalmology & Visual Science, September 2011, Vol. 52, No. 10

responses to physiologic challenges have been reported, albeit they were at low spatial resolution and without detecting layers.

The goal of this study was to investigate eye-fixation stability and high-resolution anatomic MRI of the human retina with corroboration by OCT on the same subjects. First, an optimal protocol for maintaining eye-fixation stability with cued eye blinks using an eye tracker was developed outside the scanner. Second, the size and shape of a receive-only radiofrequency (RF) detector were optimized for sensitivity in the posterior retina and different pulse sequences were explored at 3 T to achieve high spatiotemporal resolution. Third, layer-specific anatomic MRI (up to 100 × 200 × 2000 μm) of the human retina was achieved in which the subjects maintained stable eye fixation on a target with cued eye blinks, providing temporally stable MRI images. Finally, OCT with a long-wavelength (1060 nm) laser source to improve visualization of the deeper choroid layer was used to corroborate MRI layer assignments and thickness on the same eyes over matching regions around the optic nerve head (ONH) and macula.

Methods

Eye-Fixation Stability

All studies were performed with Institutional Review Board approval on four normal subjects (three males, one female; age, 24 to 45 years old). With the subject in the MRI head holder and a supine position outside the MRI scanner, the corneal position was noninvasively digitized at 240 Hz with 0.1° angular resolution using an eye tracker (ETL-500; ISCAN Inc., Woburn, MA). Subjects were instructed to maintain stable eye fixation on a target and blink immediately after data-acquisition sound cues (via playback of recorded scanner sounds). Eye-tracking data were recorded over 1.5 and 5 minutes. Two to four repeated trials were measured on each subject.

Angular displacements were converted to linear displacement at the posterior retina (1° = 291 μm) and plotted as a function of time. For quantitative analysis, data during eye blinks per se were discarded in that they were artifacts because tracking of the cornea was lost during blinks when eyelids were closed. Standard deviation of the horizontal and vertical displacements with blinks removed was computed across the time-series data.

MRI Experiments

MRI studies were performed on the same four subjects using a 3-T whole-body MRI scanner (Achieva; Philips Healthcare, Andover, MA) equipped with 80 mT/m gradient system. A custom-made, receive-only oblique eye coil of 6 × 7 cm in diameter was used. Diameter and shape of the eye coil were optimized for signal-to-noise ratio (SNR) at the posterior pole of the adult human retina. The vendor's body RF coil was used for signal excitation. Supine subjects in a custom-made, padded head holder were instructed to maintain stable eye fixation on a target with cued eye blinks immediately after data acquisition (readout gradient produced distinct sounds) during MRI. To demonstrate proof of concept, only a central axial slice bisecting the ONH and fovea was imaged to minimize partial-volume effect (PVE) due to the retinal curvature. The slice was carefully chosen through multislice pilot scans.

Time-series dynamic scans used the two-dimensional balanced steady state free precession (bSSFP) sequence.[37] Duration for each dynamic scan was 8 seconds. Careful localized shimming with high-order shims was used. Shims were adjusted if needed to "move" banding artifacts away from the region of interest: the posterior pole of the retina. The bSSFP sequence parameters were: repetition time (TR) = 20 ms, echo time (TE) = 2.1 ms, flip angle = 40°, readout bandwidth = 5.3 kHz, field of view (FOV) = 50 × 100 mm, matrix = 500 × 500 leading to a spatial resolution of 100 × 200 × 2000 μm, with the higher resolution placed along the readout direction (up-and-down on displayed images). In some measurements, 100 × 240 × 2000-μm resolution was used with a reduced matrix size. A partial Fourier readout of 51% was applied along the frequency-encoded direction, and a large FOV was used in the phase-encoding direction to eliminate aliasing artifacts. A total of 10 dynamics were acquired, resulting in an 80-second time block.

Images were analyzed using customized algorithms (MATLAB, The MathWorks Inc., Natick, MA; Functional Magnetic Resonance Imaging of the Brain Software Library, Oxford, UK). Images were acquired in time series and coregistered using customized algorithms (MATLAB). The retina was automatically detected using an edge-detection technique.[25] Radial projections perpendicular to the vitreous boundary were obtained with three- or fourfold the sampling density of the original image, and projection profiles at different time points were then coregistered to the averaged profile by minimizing the root-mean-square distances. Time-series movies of MR images were carefully evaluated to verify the absence of gross motion or drift before further analysis. Band thicknesses were determined taking the width at half height. The total retina/choroid thickness determined from MRI data was plotted as a function of distance from the ONH. The typical temporal and nasal regions analyzed were those defined later (see Fig. 4), ±2 mm beginning at ±0.5–1.0 mm away from the ONH.

Optical Coherence Tomography

OCT was recorded using a custom-made system[38] with a 34-kHz, 1060-nm swept source laser with 58-nm bandwidth (HSL-1000; Santec USA Corp., Hackensack, NJ). The system had a theoretical depth resolution of 8.5 μm in air and, after correction for refractive index of posterior ocular tissue (n = 1.38),[39] the depth resolution was 6.2 μm. Lateral resolution was 15 μm, determined by the beam diameter on the focal plane. Each B-scan consisted of 512 A-scans, providing a B-scan repetition rate of 66 Hz. Real-time feedback[38,40] was used to improve image quality by adjusting the focal plane probe beam specific to the subject's optical power and aberrations. A commercial line scanning laser ophthalmoscope (PSI Inc., Andover, MA) was incorporated into the custom-made OCT system to provide a real-time fundus image for positioning.

OCT was recorded from the same four subjects under dark adaptation without pupil dilation. To obtain a slice matching that of MRI, a central axial slice bisecting the ONH (which was visible) was recorded while the subject fixed on a target straight ahead in a sitting position. Three runs of 3.9-mm-wide B-scans were acquired from each volunteer, with the vertical B-scans placed close to the center of ONH. Each run consisted of 120 B-scans (acquisition time per run was 1.8 seconds) acquired from the same retinal location. The center of the B-scans in the first run coincided with the center of ONH. The B-scans of the second and third runs were shifted (1.5 mm) to the nasal and temporal directions, respectively. Recording multiple runs was necessary due to OCT's limited FOV. OCT images were coregistered before averaging using customized algorithms (MATLAB). OCT retinal layers were identified and assigned. The total OCT retina/choroid thickness was plotted as a function of distance from the ONH.

Results

Eye-tracking displacements of the vertical and horizontal eye movement using the eye-fixation protocol with cued blinks are shown in Figure 1. The large regular vertical deflections were those from eye blinks every 8 seconds over 1.5 minutes. The extracted segments after the eye blinks were removed (Fig. 1B) showed the displacements ranging from −150 to +150 μm. Displacement data from the 1.5- and 5-minute measurements were not statistically different and they were grouped together. The group-averaged temporal SDs of the horizontal and vertical displacements at the posterior retina were, respectively, 78 ± 51 and 130 ± 51 μm (mean ± SD, four subjects). The

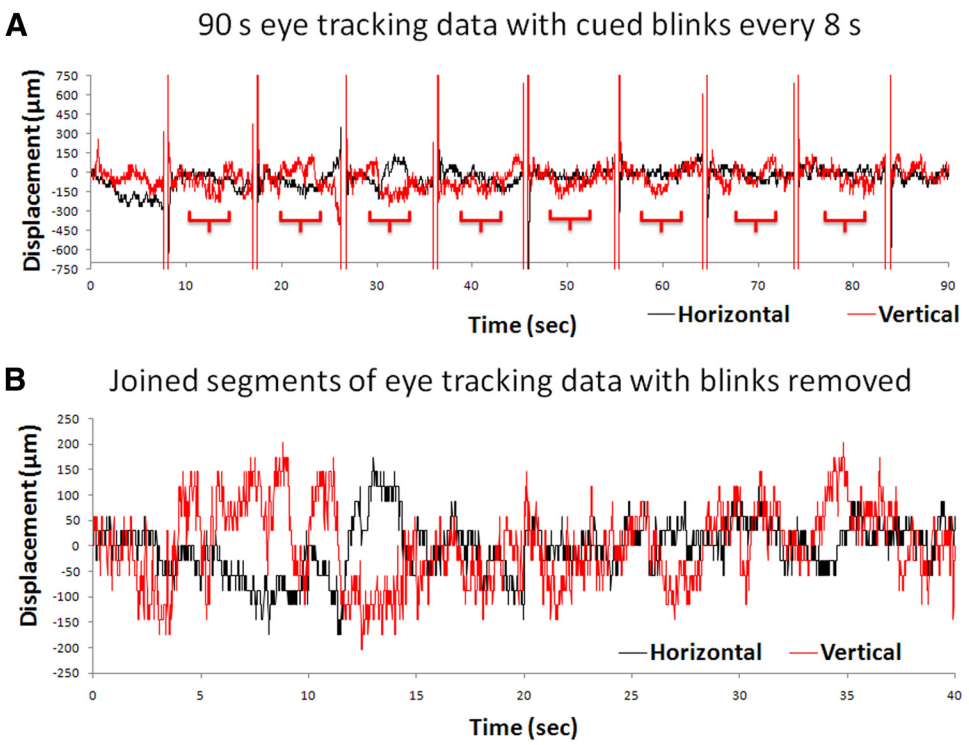

FIGURE 1. (**A**) Time courses of eye-movement displacements obtained following the eye-fixation protocol with cued blinks from one subject. Vertical and horizontal eye movements as measured using the eye-tracking device are shown over 1.5 minutes. The large regular vertical deflections are eye blinks, where the closed eyelids resulted in a loss of tracking. (**B**) The joined segments of the eye-tracking data after the blinks were removed from one subject. These segments were those derived from the brackets under the traces shown in **A**. The resolution of eye tracker is 29.6 μm.

temporal SD of the vertical displacement was larger ($P < 0.05$) than that of the horizontal displacement, as expected. Measurements on an artificial eye showed a temporally steady trace with no fluctuation and thus the temporal fluctuation in the human eye was physiologic. The displacement resolution of the eye tracker was 29.6 μm.

Time-loop movies and center-of-mass movement of the time-series MRI images showed images free of movement artifacts and were temporally stable. Coregistration was successful in correcting for minor drift and movement. On average, only 3% of the images in each time series were discarded due to eye movement during data acquisition.

Figure 2 shows a bSSFP MRI image of the human eye with 100 $\times$ 200 $\times$ 2000-μm resolution. The vitreous appeared relatively bright and the sclera behind the retina appeared relatively dark, demarcating the boundaries of the retina/choroid. Three (bright dark bright) layers within the retina/choroid complex were detected. The eye-fixation protocol with cued blinks allowed acquisition of retinal MRI data over 2 minutes consistently free of movement artifacts.

OCT was performed on the same eye (Fig. 3). All established layers of the retina, including the choroid, were visible. Based on the consistency of the human MRI data with rodent, feline, and baboon retinal MRI data all of which showed interleaving hyper-, hypo-, and hyperintense layers (see the Discussion section) the MRI layers 1–3 in the human retinas were similarly assigned to correspond to the OCT layers as shown on the figure.

The total retina/choroid thicknesses by MRI and OCT are plotted as a function of distance from the ONH (Fig. 4, one subject). The total MRI thickness was slightly larger than the total OCT thickness across all regions measured. Group-averaged MRI and OCT retina/choroid thicknesses for the three individual MRI layers from similar retinal regions for the nasal and temporal quadrants are summarized in Table 1. The combined nasal and temporal retina/choroid thickness by MRI was 711 $\pm$ 37 μm, which was 19% ($P < 0.05$) thicker than that by OCT (579 $\pm$ 34 μm).

DISCUSSION

This study demonstrates that eye fixation with cued blinks can achieve stability of the retina to within 100 μm, adequate for the MRI spatial resolution herein. MRI can achieve high spatiotemporal and layer-specific anatomic resolution of the human retina at 100 $\times$ 200 $\times$ 2000 μm at 3 T free of movement artifacts, made possible by the custom-made surface coil, high spatiotemporal resolution imaging protocol (bSSFP), optimized imaging parameters, high-order shims, a stable eye-fixation protocol with cued blinks, and image coregistration. Laminar assignments and thicknesses are corroborated by OCT on the same eyes over closely matched regions. Compared with OCT, MRI overestimates thicknesses by 19%, likely a result of MRI's PVE. These initial results encourage further development to improve spatiotemporal resolution for anatomic MRI, and explore layer-specific blood-flow, and blood-oxygenation dependent MRIs.

Eye-Fixation Stability

The average time period between human eye blinks is approximately 5 seconds. In exploratory trials outside the MRI scanner, we found that a blinking period of 4 to 8 seconds was comfortable for the normal subjects. Pulse sequence parameters were thus adjusted such that the dynamic time of each scan was within this range of blinking rate (~4.6 seconds). The temporal SD of the displacement with our fixation protocol was on the order of 100 μm. Stability of the MRI time-series data is consistent with that of the eye-tracker data. Only 3% of the images in each time series were discarded due to eye movement during data acquisition. With expected improvement in MRI spatial resolution, improvement on eye-fixation stability with trained eye fixation may be necessary, and this is currently being explored.

Layer Thicknesses and Assignment

Previous studies of rodent[25] and feline[14] retinas revealed three layers of alternative hyper-, hypo-, and hyperintensity. These

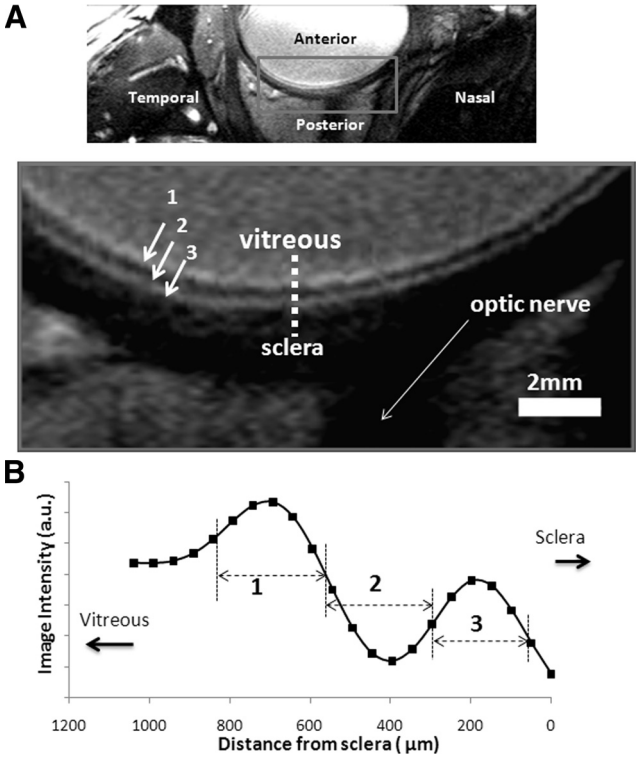

FIGURE 2. (**A**) A bSSFP MRI of the human eye with 100 × 200 × 2000-μm resolution at 3 Tesla. The vitreous appeared relatively bright and the sclera behind the retina appeared relatively dark. Laminar structures within the retina/choroid show three layers of hyper-, hypo, and hyperintense strips (layers 1–3). (**B**) A spatial profile taken across the retinal thickness from vitreous to sclera.

data were obtained using conventional T_1- and/or T_2-weighted sequences on a 4.7- and a 7-T animal scanner, where gradient strengths (40 G/cm) were much stronger than those on clinical scanners. Strong gradients allowed a small FOV and shorter readout time, yielding a resolution of 60 × 60 × 1000 μm for rodent retina[25] and 100 × 100 × 2000 μm for feline retina.[14] Retinal MRI of the anesthetized baboon retina at 100 × 200 × 2000 μm on a clinical 3-T scanner has also been reported,

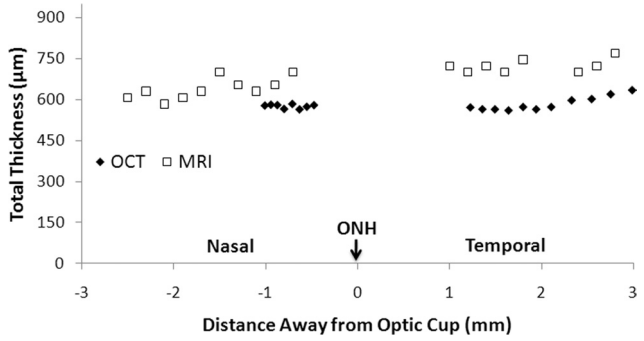

FIGURE 4. Total retina/choroid thickness as a function of distance from the ONH by MRI and optical coherence tomography on the same subject.

demonstrating hardware feasibility of high spatiotemporal resolution anatomic, blood-flow, and BOLD MRIs on a 3-T clinical scanner.[31] Anatomic MRI of the baboon retina also revealed a similar three layers of alternative hyper-, hypo-, and hyperintensity. The total retina/choroid thicknesses (in μm) of the rodent, feline, baboon, and human retinas have been reported to be, respectively, 267 ± 33,[25] 358 ± 13,[14] 617 ± 101,[31] and 711 ± 37 (this study) (mean ± SD).

We were encouraged by the spatial resolution of 100 × 200 × 2000 μm in the human retina, given that the human eye is significantly larger in diameter and the human retina is significantly thicker compared with that of rodents. The PVE due to the curvature of the human retina for the 2000-μm-thick MRI slice is negligible (~5% of total thickness),[25] whereas a 600-μm-thick slice in the rodent retina is needed to yield the same 5% PVE.[25] For the in-plane resolution, 100 × 200 μm yielded 6.6 × 3.3 pixels across the human retina/choroid thickness. The higher resolution was placed along the thickness of the posterior pole of the retina. By comparison, 60 × 60-μm in-plane resolution in rodent retina yielded 4.5 × 4.5 pixels across the retinal thickness.[25] Thus, the MRI resolution of the human retina was overall favorable, or at least comparable, to those used in animal studies, despite the apparent hardware limitations and eye movement in awake humans. MR images of the human retina, however, appeared more blurry than those of rodents, felines, and baboons. This is likely due to

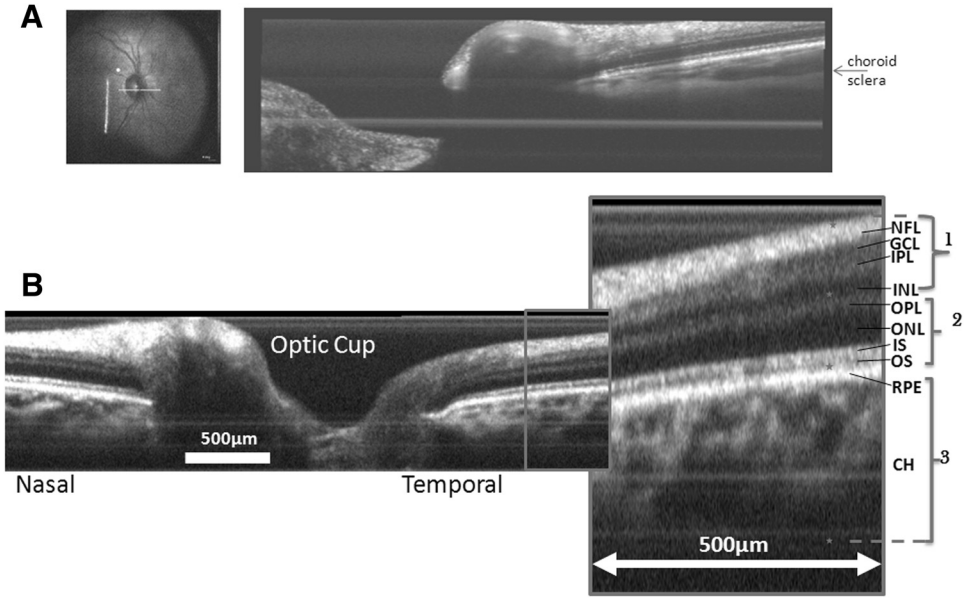

FIGURE 3. Optical coherence tomography around the optic cup with parameters optimized to visualize (**A**) the deeper choroid and (**B**) overall retina/choroid. NFL, nerve fiber layer; IPL, inner plexiform layer; OPL, outer plexiform layer; IS/OS, inner/outer photoreceptor segment layer; RPE, retinal pigment epithelium; CH, choroidal vascular layer. The *asterisk* indicates roughly the boundaries between adjacent layers as in MRI.

TABLE 1. Thickness of MRI Layers and the Corresponding OCT Layers of the Human Retina (mean ± SD, $n = 4$)

	Temporal Thickness		Nasal Thickness		Average Thickness	
Layer	MRI (μm)	OCT (μm)	MRI (μm)	OCT (μm)	MRI (μm)	OCT (μm)
1	197 ± 62	236 ± 29	254 ± 50	223 ± 36	226 ± 53	229 ± 30
2	248 ± 48*	117 ± 16*	220 ± 42*	110 ± 12*	234 ± 31*	114 ± 10*
3	243 ± 48	256 ± 39	260 ± 77	216 ± 25	251 ± 48	236 ± 21
Total	688 ± 85*	608 ± 73*	734 ± 69*	549 ± 29*	711 ± 37*	579 ± 37*

The temporal and nasal regions analyzed were those defined in Figure 4, approximately ±2 mm, beginning at ±0.5–1 mm away from the optic nerve head. Asterisks indicate statistical significance between MRI and OCT retina/thickness thicknesses: * $P < 0.05$ two-tailed paired *t*-test.

the long readout time used to maximize signal sensitivity and this problem must be addressed in future studies.

MRI data of rodent,[25] feline,[14] and baboon[31] retinas all showed three layers of alternating hyper-, hypo-, and hyperintensity, despite different pulse sequences and parameters. Specifically, the baboon and human retinal data both used the bSSFP sequence, yielded similar interleaving hyper-, hypo-, and hyperintensity in the retina. bSSFP is more efficient and yielded better SNR per unit time compared with conventional gradient-echo sequences. Based on these similarities in MRI layers across different animal species, similar layer assignments were thus made. Layer 1 (hyperintense) closest to the vitreous likely corresponded to nerve fiber, ganglion cell, and INL; layer 2 (hypointense) strip likely corresponded to the ONL and inner and outer segments; layer 3 (hyperintense) likely corresponded to the choroid.

Unlike animal studies where layer assignment and thickness of the MRI bands could be cross-validated by histology, direct validation of human layer assignments and thicknesses is difficult. Thus, noninvasive OCT was used to corroborate total retina/choroid thickness on the same eyes over closely matched regions. Commercial OCT devices use an 800- to 850-nm wavelength light source, where the choroid is difficult to visualize due to strong tissue absorption/scattering of visible light. The OCT device in our study used a less common, longer-wavelength (1060 nm) laser with less tissue absorption and scattering, which allowed better visualization of the deeper choroid layer.[41] Our OCT data are in general agreement with published OCT data. The published thickness of the in vivo human neural retina (excluding the choroid) varied significantly, even within the OCT literature: 236 μm[42] and 200 to 310 μm.[43] This is likely due to the heterogeneity of the human populations and different regions of the retinas from which the thickness were derived. Reports of the in vivo human choroidal thickness are sparse but have been reported to be 293 to 307 μm by partial coherence interferometry[44] and 318 to 335 μm by OCT.[45] Together, the total retinal thickness including the choroid ranged from 500 to 650 μm in the literature.[42–45]

In our study, retina/choroid thickness measured by MRI was greater than that determined by OCT over a similar region of the same eye, likely because MRI PVE overestimates layer thicknesses. PVE can be minimized by increasing spatial resolution and suppressing the vitreous signals. The uncertainty in identifying the outer choroidal boundary by OCT as well as errors in estimating the refractive index or direction of light travel could also contribute to the apparent discrepancy in OCT thickness. Finally, it should be noted that the retinal layer thicknesses vary considerably depending on location.

Drawbacks and Challenges of Retinal MRI

Compared with anatomic MRI of the retina, OCT offers higher spatiotemporal resolution and is cost effective. Most optical imaging methods provide only anatomic data and they can also be hindered by media. With the exception of OCT for anatomic imaging, optical imaging techniques are depth ambiguous. MRI, by contrast, is not depth limited and, importantly, offers physiologic data as well as quantitative parameters. BOLD fMRI in response to physiologic challenges[36] and blood-flow MRI of basal conditions[34,35] and during physiologic challenges[35] of the human retinas have recently been reported. These MRI approaches have the potential to provide valuable tools to study neurovascular coupling and functional responses, which may be perturbed in early stages of retinal diseases, as documented in many neurologic diseases. Future studies will use multislice or three-dimensional MRI to image the entire retina and present images in en face view. Improving contrast and resolution is necessary to visualize major retinal layers. A recent bSSFP MRI study on anesthetized mice could detect additional anatomic layers and layer-specific "physiologically evoked" BOLD responses.[46] Similarly, MRI of layer-specific, quantitative retinal and choroidal blood flow in the rodent retina is feasible.[22] MRI provides blood-flow values with classical units reflecting tissue perfusion, in contrast to blood-cell velocity measurements in large vessels often measured using optical approaches.

CONCLUSIONS

In conclusion, this study reports high-resolution MRI of lamina-specific structures in the unanesthetized human retina. Although further improvement in spatiotemporal resolution is necessary and expected, these initial results encourage further developments of additional MRI applications to study the human retina. We predict that MRI has the potential to offer some unique layer-specific physiologic data that are depth-resolved and quantitative, potentially complementing existing retinal imaging techniques.

Acknowledgments

The authors thank Carlos Rosende, MD, for many helpful discussions.

References

1. Wassle H, Boycott BB. Functional architecture of the mammalian retina. *Physiol Rev.* 1991;1:447–480.
2. Harris A, Kagemann L, Cioffi GA. Assessment of human ocular hemodynamics. *Surv Ophthalmol.* 1998;42:509–533.
3. Webb RH, Hughes GW. Scanning laser ophthalmoscope. *IEEE Trans Biomed Eng.* 1981;28:488–492.
4. Fujimoto JG, Pitris C, Boppart SA, Brezinski ME. Optical coherence tomography: an emerging technology for biomedical imaging and optical biopsy. *Neoplasia.* 2000;2:9–25.
5. Preussner PR, Richard G, Darrelmann O, Weber J, Kreissig I. Quantitative measurement of retinal blood flow in human beings

by application of digital image-processsing methods to television fluorescein angiograms. *Graefes Arch Clin Exp Ophthalmol.* 1983; 221:110–112.

6. Blair NP, Feke GT, Morales-Stoppello J, et al. Prolongation of the retinal mean circulation time in diabetes. *Arch Ophthalmol.* 1982; 100:764–768.
7. Guyer DR, Yannuzzi LA, Slakter JS, Sorenson JA, Orlock S. The status of indocyanine-green videoangiography. *Curr Opin Ophthalmol.* 1993;4:3–6.
8. Schmidt-Erfurth U. Indocyanine green angiography and retinal sensitivity after photodynamic therapy of subfoveal choroidal neovascularization. *Semin Ophthalmol.* 1999;144:35–44.
9. Cheng H, Duong TQ. Simplified laser-speckle-imaging analysis method and its application to retinal blood flow imaging. *Opt Lett.* 2007;32:2188–2190.
10. Cheng H, Yan Y, Duong TQ. Temporal statistical analysis of laser speckle image and its application to retinal blood-flow imaging. *Opt Express.* 2008;16:10214–10219.
11. Tsunoda K, Oguchi Y, Hanazona G, Tanifuji M. Mapping cone- and rod-induced retinal responsiveness in macaque retina by optical imaging. *Invest Ophthalmol Vis Sci.* 2004;45:3820–3826.
12. Grinvald A, Bonhoeffer T, Vanzetta I, et al. High-resolution functional optical imaging: from the neocortex to the eye. *Ophthalmol Clin North Am.* 2004;17:53–67.
13. Shonat RD, Richmond KN, Johnson PC. Phosphorescence quenching and the microcirculation: An automated, multipoint oxygen tension measuring instrument. *Rev Sci Instrum.* 1995;66:5075–5084.
14. Shen Q, Cheng H, Pardue MT, et al. Magnetic resonance imaging of tissue and vascular layers in the cat retina. *J Magn Reson Imaging.* 2006;23:465–472.
15. Chen J, Wang Q, Zhang H, et al. In vivo quantification of T(1), T(2), and apparent diffusion coefficient in the mouse retina at 11.74T. *Magn Reson Med.* 2008;59:731–738.
16. Nair G, Shen Q, Duong TQ. Relaxation time constants and apparent diffusion coefficients of rat retina at 7 Tesla. *Int J Imaging Syst Technol.* 2010;20:126–130.
17. Berkowitz BA, Roberts R, Goebel DJ, Luan H. Noninvasive and simultaneous imaging of layer-specific retinal functional adaptation by manganese-enhanced MRI. *Invest Ophthalmol Vis Sci.* 2006;47: 2668–2674.
18. Nair G, Pardue MT, Kim M, Duong TQ. Manganese-enhanced MRI reveals multiple cellular and vascular layers in normal and degenerated retinas. *J Magn Reson Imaging.* In press.
19. Duong TQ, Pardue MT, Thule PM, et al. Layer-specific anatomical, physiological and functional MRI of the retina. *NMR Biomed.* 2008;21:978–996.
20. Li Y, Cheng H, Duong TQ. Blood-flow magnetic resonance imaging of the retina. *NeuroImage.* 2008;39:1744–1751.
21. Li Y, Cheng H, Shen Q, et al. Blood-flow magnetic resonance imaging of retinal degeneration. *Invest Ophthalmol Vis Sci.* 2009; 50:1824–1830.
22. Muir ER, Duong TQ. MRI of retinal and choroid blood flow with laminar resolution. *NMR Biomed.* 2011;24:216–223.
23. Shih YY, De La Garza BH, Muir ER, et al. Lamina-specific functional MRI of retinal and choroidal responses to visual stimuli. *Invest Ophthalmol Vis Sci.* 2011;52:5303–5310.
24. Nair G, Tanaka Y, Kim M, et al. MRI reveals differential regulation of retinal and choroidal blood volumes in rat retina. *NeuroImage.* 2011;54:1063–1069.
25. Cheng H, Nair G, Walker TA, et al. Structural and functional MRI reveals multiple retinal layers. *Proc Natl Acad Sci USA.* 2006;103: 17525–17530.
26. Duong TQ, Ngan S-C, Ugurbil K, Kim S-G. Functional magnetic resonance imaging of the retina. *Invest Ophthalmol Vis Sci* 2002; 43:1176–1181.
27. De La Garza B, Li G, Muir E, Shih YY, Duong TQ. BOLD fMRI of visual stimulation in the rat retina at 11.7 Tesla. *NMR Biomed.* 2011;24:188–193.
28. Berkowitz BA, Roberts R, Luan H, Peysakhov J, Mao X, Thomas KA. Dynamic contrast-enhanced MRI measurements of passive permeability through blood retinal barrier in diabetic rats. *Invest Ophthalmol Vis Sci.* 2004;45:2391–2398.
29. Calkins DJ, Horner PJ, Roberts R, Gradianu M, Berkowitz BA. Manganese-enhanced MRI of the DBA/2J mouse model of hereditary glaucoma. *Invest Ophthalmol Vis Sci.* 2008;49:5083–5088.
30. Chan KC, Fu QL, Hui ES, So KF, Wu EX. Evaluation of the retina and optic nerve in a rat model of chronic glaucoma using in vivo manganese-enhanced magnetic resonance imaging. *NeuroImage.* 2008;40:1166–1174.
31. Zhang Y, Wey H-Y, Nateras OS, Peng Q, De La Garza BH, Duong TQ. Anatomical, blood oxygenation level-dependent, and blood flow MRI of nonhuman primate (baboon) retina. *Magn Reson Med.* 2011;66:546–554.
32. Berkowitz BA, McDonald C, Ito Y, Tofts PS, Latif Z, Gross J. Measuring the human retinal oxygenation response to a hyperoxic challenge using MRI: eliminating blinking artifacts and demonstrating proof of concept. *Magn Reson Med.* 2001;46:412–416.
33. Richdale K, Wassenaar P, Teal Bluestein K, et al. 7 Tesla MR imaging of the human eye in vivo. *J Magn Reson Imaging.* 2009; 30:924–932.
34. Maleki N, Dai W, Alsop DC. Blood flow quantification of the human retina with MRI. *NMR Biomed.* 2011;24:104–111.
35. Peng Q, Zhang Y, Nateras OSE, van Osch MJP, Duong TQ. MRI of blood flow of the human retina. *Magn Reson Med.* 2011;65:1768–1775.
36. Zhang Y, Peng Q, Kiel JW, Rosende CA, Duong TQ. Magnetic resonance imaging of vascular oxygenation changes during hyperoxia and carbogen challenges in the human retina. *Invest Ophthalmol Vis Sci.* 2011;52:286–291.
37. Scheffler K, Lehnhardt S. Principles and applications of balanced SSFP techniques. *Eur Radiol.* 2003;13:2409–2418.
38. Elmanaoui B. *Swept Source Polarization Sensitive Optical Coherent Tomography for Retinal Imaging at 1 Micron*. Austin, TX: University of Texas at Austin; 2010. Thesis.
39. Hariri S, Moayed AA, Dracopoulos A, Hyun C, Boyd S, Bizheva K. Limiting factors to the OCT axial resolution for in-vivo imaging of human and rodent retina in the 1060 nm wavelength range. *Opt Express* 2009;17:24304–24316.
40. Kuranov RV, McElroy AB, Kemp N, et al. Gas-cell referenced swept source phase sensitive optical coherence tomography. *Photon Technol Lett*. 2010;22:1524–1526.
41. Povazay B, Hofer B, Torti C, et al. Impact of enhanced resolution, speed and penetration on three-dimensional retinal optical coherence tomography. *Opt Express.* 2009;17:4134–4150.
42. Schuman JS, Hee MR, Puliafito CA, et al. Quantification of nerve fiber layer thickness in normal and glaucomatous eyes using optical coherence tomography. *Arch Ophthalmol.* 1995;113:586–596.
43. Alamouti B, Funk J. Retinal thickness decreases with age: an OCT study. *Br J Ophthalmol.* 2003;87:899–901.
44. Salzmann M, Brown EVL. *The Anatomy and Histology of the Human Eyeball in the Normal State: Its Development and Senescence.* Chicago: The University of Chicago Press; 1912.
45. Spaide RF, Koizumi H, Pozzoni MC. Enhanced depth imaging spectral-domain optical coherence tomography. *Am J Ophthalmol.* 2008;146:496–500.
46. Muir ER, Duong TQ. Layer-specific functional and anatomical MRI of the retina with passband balanced SSFP. *Magn Reson Med.* In press.